CHAPTER-5

Synthesis and characterizations of $MnMoSe_2$/ppy heterostructures as advanced catalysts for alkaline water oxidation: enhanced OER activity and mechanistic insights via *operando* spectroscopy

5.1. Abstract

The development of reliable and economically viable functional catalysts for alkaline water oxidation is crucial for progressing electrocatalytic water splitting technologies. This article outlines a novel strategy utilizing a distinctive heterostructure catalyst, carefully crafted to improve efficiency in OER. Through a sophisticated hydrothermal synthesis method followed by solid state grinding, we have synthesized a novel $MnMoSe_2$/ppy material showcasing enhanced electrocatalytic properties and numerous active sites, which effectively reduces overpotential. The morphological and crystal structure of the $MnMoSe_2$/ppy catalyst was determined utilizing high resolution transmission electron microscopy (HR-TEM), field-emission scanning electron microscopy (FE-SEM), and powder X-ray diffraction (PXRD). The outcomes indicate that the $MnMoSe_2$/ppy composite demonstrates exceptional catalytic performance, starting OER at a notably lesser overpotential of 205 mV (vs. RHE) at 10 mA cm^{-2} current density (η_{10}), accompanied by a Tafel slope of 70 mV dec^{-1}. The *operando* UV-Vis spectro-electrochemical analysis sheds light on the active intermediate species that participate in the OER, offering important insights into the catalytic mechanism. This study presents a novel high-performance catalyst and marks a considerable progression in renewable energy technology development, providing a viable solution for sustainable energy applications.

5.2. Introduction

Non-renewable fossil fuels have served as the backbone of modern energy systems, including natural gas, coal, and petroleum, significantly influencing the structure of contemporary

society [1]. Nonetheless, the significant dependence on fossil fuels has resulted in negative environmental consequences and increased global consciousness regarding possible energy crises [2–4]. This has created an essential demand to explore non-conventional fuel options, such as hydropower, tidal, solar, and wind energy, as substitutes for fossil fuels [5]. Although these renewable sources hold great potential, they frequently encounter challenges related to their intermittency, which affects their practical applications [6]. The combination of these challenges and the non-toxicity of hydrogen has led to considerable investigation into hydrogen as an energy source, which features a greater gravimetric energy density of 120 MJ kg^{-1} [6,7]. Noted for its exceptional energy conversion efficiency, hydrogen is progressively regarded as a crucial future energy resource that can fulfill the needs of an expanding modern society [8,9].

In context to the growing need for hydrogen fuel, alkaline water electrolysis has surfaced as a practical technique for generating hydrogen energy on an industrial scale [10,11]. This technique includes two half-cell reactions in the context of water splitting: the anodic oxygen evolution reaction (OER) and the cathodic hydrogen evolution reaction (HER) [11]. Often referred to as the “heart” of electrochemical water splitting, the OER is essential yet presents challenges due to its slow kinetics and the requirement of a thermodynamic potential of 1.23 V to finish a four-electron ($4e^-$) transfer, making it the rate-limiting step in the process [12,13].

Several investigations have emphasized the significance of active edge sites for catalytic activity in transition metal dichalcogenides (TMDCs), showing that doping and morphological control may efficiently optimize these sites. In the OER, these alterations may

improve TMDC performance by enhancing the density of active sites and boosting electrical conductivity [14,15]. In contrast to their bulk counterparts, structural flaws have a major impact on low-dimensional materials and are crucial in defining their optical, magnetic, and electrical properties [16,17]. Metal doping creates vacancies of sulfur or selenium on the margins of TMDC layers, which are the main sites for electrocatalytic activity. This enhances the quantity of active catalytic sites [18]. Furthermore, metal doping creates catalytic edges by introducing unbalanced Coulomb pressures that cause atomic rearrangement and defect formation [19,20]. This improvement of active edges encourages OER activity and speeds up electron transfer [21,22]. The density of active catalytic sites may be increased by transition metal doping [18], which has the ability to activate basal planes, which are typically less electrocatalytically active than edge sites. Moreover, edge site activity may be greatly increased by defect engineering on the basal planes [23].

Due of the fascinating electrical and antiferromagnetic characteristics, $MnSe_2$ has drawn interest in a variety of industries, including optoelectronics, semiconductors, and photovoltaics [24]. Its magneto-optical properties, which result from intense sp-d exchange processes involving electron-hole band states and the 3d electronic states of Mn^{2+} ions, are primarily responsible for this interest [25]. With Mn atoms occupying octahedral sites and associating with Se atoms at tetrahedral sites, $MnSe_2$ is structurally a member of the pyrite crystal family [26]. Due to their widespread availability and abundant natural occurrence, $MnSe_2$ and its hybrid derivatives have recently gained attention from several research groups worldwide as they investigate these materials for improved functional qualities across a range of applications [27,28].

According to recent studies, catalyst materials' electrochemical performance may be greatly improved by adding certain transition metal ions [29]. These dopants cause structural flaws in the host material and open up additional catalytic sites [30]. Doping improves the overall electrocatalytic efficiency of transition metal-based catalysts while also effectively increasing intrinsic activity and dispersing local charge density [31,32]. Because of their stability and advantageous catalytic qualities, molybdenum-based catalysts, including molybdenum carbide, nitride, and sulfide, have garnered a lot of attention [33,34]. Transition metals such as copper, nickel, cobalt, manganese, zinc, and molybdenum have all been used as dopants [35], with molybdenum being particularly well-known for its capacity to greatly enhance charge transport, electrical conductivity, and catalytic activity [36].

In this work, a conductive polymer polypyrrole (ppy) is added to the catalyst system which enhances the OER functionality of $MnMoSe_2$. ppy is a five-membered C–N heterocyclic structure with an alternating single-double bond conjugation. It is extensively studied and utilized in electrochemical processes such as oxygen reduction reaction (ORR), supercapacitors, and OER [37–39]. Conductivity is greatly increased by adding ppy to the catalysts, which facilitates effective electron transport during the OER and improves overall electrocatalytic activity [40].

By concentrating on metal selenide components, we want to improve the conductivity, OER catalytic efficiency, and structural stability of composite electrocatalysts using an approach of the metal and conductive polymer doping. Research shows that when mixed with metal chalcogenides, stable conducting polymers like polypyrrole (ppy) have a high water-splitting potential. Because of its high porosity and special hybrid heterostructural interface,

which together maximize electron transport and active site accessibility, the $MnMoSe_2$/ppy catalyst exhibits exceptional OER electrocatalytic activity.

5.3. Experimental

5.3.1. Materials

Se powder (AR, Merck, 99.9%), Sodium Molybdate dihydrate ($Na_2MoO_4 \cdot 2H_2O$) (AR, Merck, 99.9 %), Hydrazine hydrate ($N_2H_4.xH_2O$), Manganese Chloride hexahydrate ($MnCl_2 \cdot 6H_2O$) (AR, Merck, 99.9 %), and Pyrrole (AR, Merck, 99.9%).

5.3.2. Synthesis of $MnMoSe_2$

$MnMoSe_2$ was prepared using hydrothermal technique. In this step, 0.33 mmol of manganese chloride hexahydrate and 0.33 mmol of sodium molybdate dihydrate were completely dispersed in 20 mL of ultra-pure milli Q water and vigorously mixed using magnetic stirrer for 15 minutes. Following that, 0.11 g of selenium powder was then added to the mixture and stirred for next 30 minutes. Further, 10 mL of $N_2H_4 \cdot xH_2O$ was then added dropwise, resulting in a dark precipitate. The mixture was then exposed to continuous magnetic stirring for two hours. This mixture was transferred to a 50 mL Teflon-lined autoclave and heated in a hot-air oven for 12 hours at 180 ^oC. After the completion of reaction, the autoclave was then allowed to cool automatically to room temperature, and the precipitate was carefully washed with water and ethanol multiple times before drying overnight at 45 ^oC.

5.3.3. Synthesis of polypyrrole

The pyrrole monomer was maintained in an inert atmosphere to prevent oxidation. 50 mL of deionized water was mixed with 0.4 mL of pyrrole monomer for synthesis, and the mixture was gently shaken to guarantee even dispersion. Then, in a nitrogen atmosphere, 50 mL of an aqueous solution of anhydrous ferric chloride was added dropwise while being constantly stirred. For six hours, the polymerization process was maintained at a temperature between 0 to 5 °C. After filtering and washing the resulting polypyrrole with double distilled water and methanol until its pH was neutral, it was vacuum-dried for 12 hours at 60 °C.

5.3.4. Synthesis of $MnMoSe_2$/ppy composite

A solid-state technique for synthesis was used to synthesize the material composite. For two to three hours, equal parts of the formed $MnMoSe_2$ and polypyrrole were placed in a mortar and thoroughly ground. To attain total homogeneity, this mixture was subsequently ultrasonically treated for an hour in an ethanol solution. The preparation process was completed by drying the composite at 45 °C.

5.3.5. fabrication of working electrode

Fluorine-doped tin oxide (FTO) acted as the supporting layer for the working electrode. In order to yield the catalyst ink, 1 mg of the synthesized catalyst was dispersed in 10 µL of 5 % Nafion solution, 20 µL of double-distilled water, and 40 µL of ethyl alcohol. The product was then ultrasonically dissolved for approximately an hour to guarantee uniform dispersion. After that, 20 µL of the catalyst ink was drop-casted onto the FTO substrate in small droplets, which were subsequently allowed to dry at room temperature.

5.3.6. Electrode fabrication for spectro-electrochemical study

The working electrode for *operando* spectro-electrochemical analysis was made using the produced catalyst ink aforementioned above. To prepare it for use as the study's working electrode, the platinum grid was submerged in the catalyst ink and then allowed to dry at room temperature.

5.4. Characterizations

5.4.1. Physicochemical characterizations

The amorphous and crystalline character of the prepared catalysts were analyzed using powder X-ray diffraction (XRD) on a Rigaku Smart Lab 9 kW powder type at a wavelength of 1.514 A°. Nova Nano-SEM for field emission-scanning electron microscopy (FE-SEM), and Thermo Fisher Technai 20 G^2 for HR-TEM were employed to understand the morphologies and microstructures of the materials. Additionally, elemental mapping and EDS analysis give an insight to the elemental composition of the prepared catalysts.

5.4.2. Electrochemical characterizations

For electrochemical investigations, three electrodes were employed in a single-compartment Pyrex glass cell. Pt foil (Aldrich 99.9% pure) having an area of 8 cm^2 serves as the counter electrode, whereas FTO/catalyst, having a working surface area of 0.5 cm^2 serves as the working electrode. All potentials were compared to the standard potential ($E^0_{Hg/HgO}$), which is 105.3 mV vs. NHE, using the Hg/HgO/1 M KOH reference electrode [41]. To link the cell electrolyte to the reference electrode, a Luggin capillary salt bridge was made ready with the

use of KCl and agar-agar. Electrochemical characterization techniques, include various methods such as, cyclic voltammetry, impedance tests, and Tafel polarization investigations, were conducted by using CHI-608C instrument (CH instrument, USA) [42–44]. To relate potential values measured by the Hg/HgO reference electrode to the reversible hydrogen electrode (RHE), **Equation 3.1** could be used which is already discussed in **Chapter 3**.

$$E_{RHE} = E_{Hg/HgO} + 0.0592 \times pH + E^{0}_{Hg/HgO} \quad \textbf{(3.1)}$$

5.4.3. Spectro-electrochemical characterizations

Platinum wire served as the counter electrode, while the catalyst ink-immersed platinum grid served as the working electrode for spectro-electrochemical analyses conducted within a quartz cuvette. The reference electrode was made of Hg/HgO in a solution of 1 M KOH. Agar-agar and KCl were used to create a Luggin capillary salt bridge, which made it easier to link the cell electrolyte and reference electrode. Spectra were acquired closest to the onset potential using LSV technique, which was swept at 5 mV s^{-1} scan rate. The Ocean Optics FLAME-T-XR1-ES Assembly was used to perform *operando* spectro-electrochemical investigations spanning a wavelength range of 200 nm to 1025 nm.

5.5. Results and discussion

5.5.1. Physicochemical characterizations

5.5.1.1. XRD

Figure 5.1 illustrates the X-ray diffraction (XRD) patterns of the composite material, polypyrrole (ppy) and $MnMoSe_2$ catalysts. The broad peak at low angles **(Figure 5.1 (a))** seen

in the XRD patterns validate the amorphous nature of the ppy component [45]. The crystalline properties of Mo doped $MnSe_2$ ($MnMoSe_2$) were analyzed using XRD. The XRD pattern of $MnMoSe_2$ has a prominent diffraction peak at 12.5°, corresponding to the (002) crystalline lattice plane which is well indexed with JCPDS card no. 653999 and confirms the hexagonal lattice structure [46]. Furthermore, the XRD peaks around 32° and 46° corresponds to $MoSe_2$ phase [47]. Clearly, $MnMoSe_2$/ppy consists of crystalline as well as amorphous peaks and does not exhibit any supplementary diffraction peaks beyond those identified in pure $MnMoSe_2$.

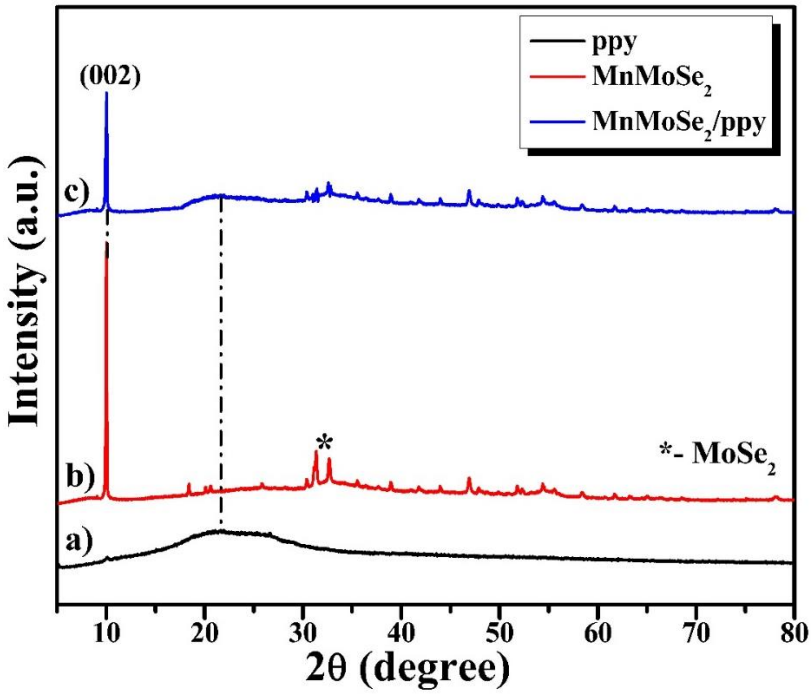

Figure 5.1. XRD patterns of **a)** ppy, **b)** $MnMoSe_2$, **c)** $MnMoSe_2$/ppy.

5.5.1.2. FE-SEM

The morphological studies of the $MnMoSe_2$/ppy composite was elucidated with the help of FE-SEM at different magnifications, which is clearly shown in **Figure 5.2 (a) and (b)**. The

FE-SEM images display a unique cuboidal rod-shaped structure having a distinctly rugged surface, a characteristic mainly related to the inclusion of ppy. The introduction of the ppy layer results in considerable surface roughness within the $MnMoSe_2$ structure, thereby effectively improving the active surface area of the composite, which are critically important for improving OER catalysis. It enables better interaction between the composite and the electrolyte. Furthermore, the FE-SEM analysis indicates that individual $MnMoSe_2$/ppy composite units are evenly distributed, exhibiting minimal agglomeration, which further reinforces the material's suitability for OER applications [48].

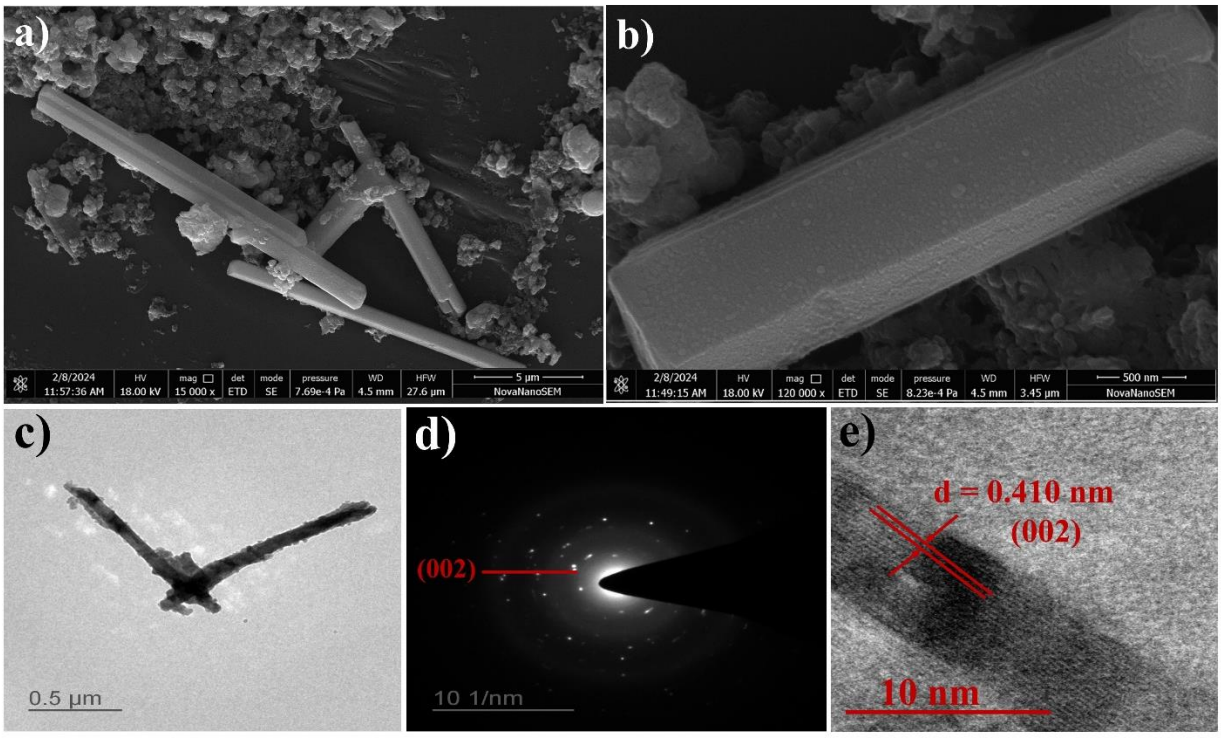

Figure 5.2. a, b) FE-SEM micrographs of $MnMoSe_2$/ppy at different magnifications, **c)** TEM micrograph of $MnMoSe_2$/ppy, **d)** SAED pattern, **e)** HR-TEM image of $MnMoSe_2$/ppy.

Furthermore, the analysis conducted through EDS as detailed in **Table 5.1**, along with the elemental mapping results illustrated in **Figures 5.3 and 5.4**, offers additional validation of these findings. The EDS data confirms the elemental composition of the $MnMoSe_2$/ppy composite, consistent with anticipated values and supporting the presence of polypyrrole on the surface. Elemental mapping provides a visual depiction of the uniform distribution of each element throughout the composite. This uniform elemental dispersion supports the structural integrity of the $MnMoSe_2$/ppy material and affirms its enhanced surface morphology, which is critical for optimizing OER efficiency.

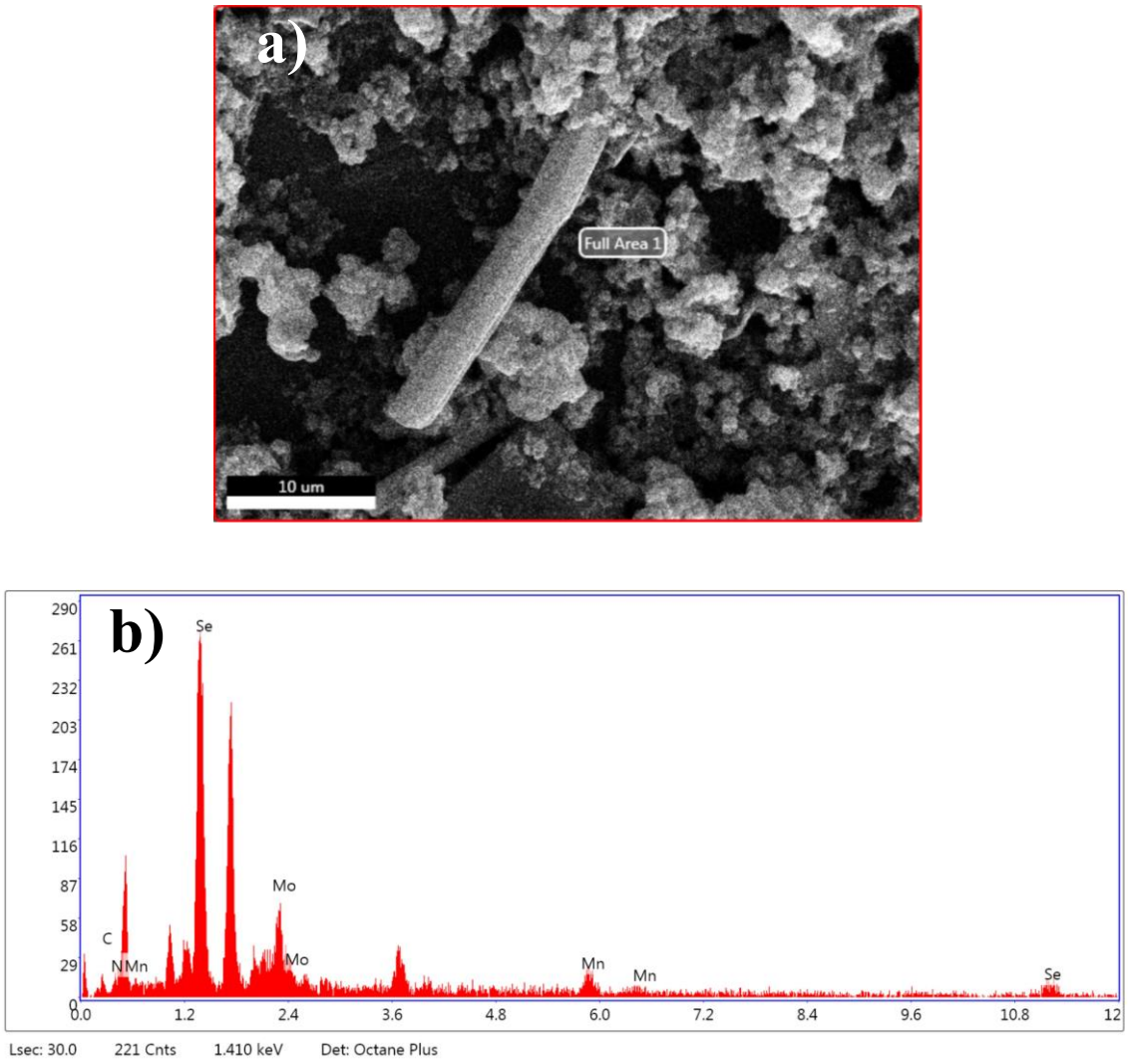

Figure 5.3. a) FE-SEM image of $MnMoSe_2$/ppy, **b)** Corresponding EDS spectra.

Table 5.1. Elemental composition from EDS spectra

Element	Weight %	Atomic %	Net Int.	Error %	Kratio	Z	A	F
C K	6.56	21.64	2.75	26.02	0.0225	0.8669	0.3951	1.0000
N K	13.26	37.55	4.41	21.60	0.0397	0.8334	0.3591	1.0000
SeL	46.34	23.27	56.73	5.58	0.2884	0.5554	1.1200	1.0003
MoL	22.36	9.24	19.51	11.13	0.1239	0.5562	0.9966	1.0000
MnK	11.49	8.29	7.66	22.82	0.0794	0.6649	0.9932	1.0468

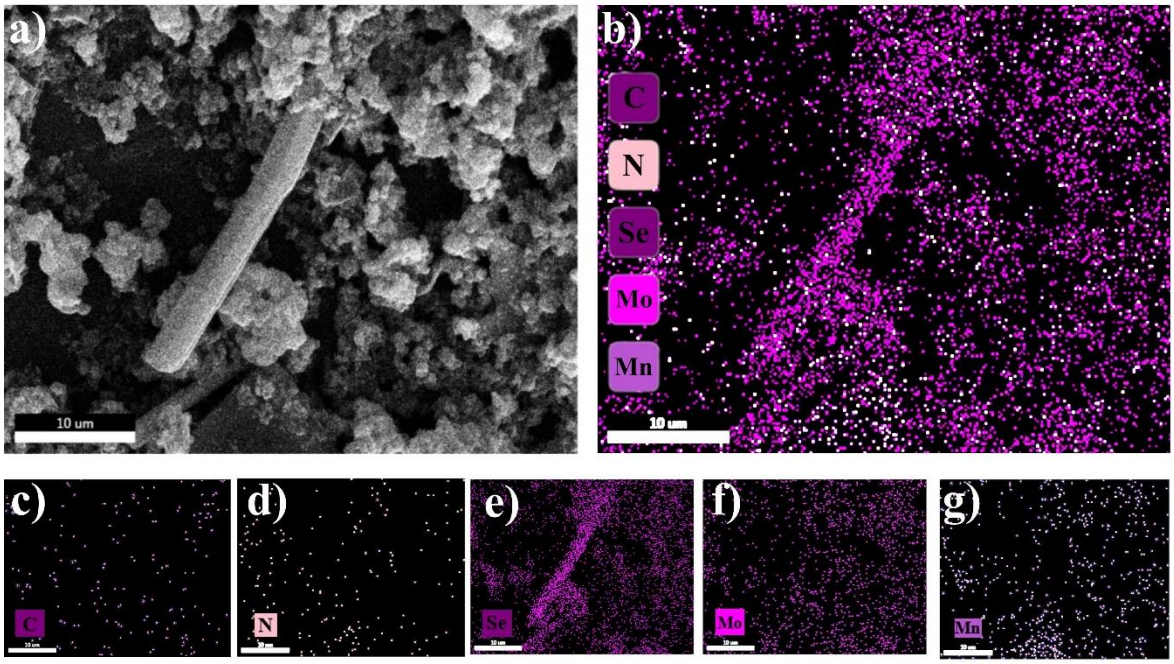

Figure 5.4. Elemental mapping.

5.5.1.3. HR-TEM

The unique microstructure of the $MnMoSe_2$/ppy composite, as shown in **Figure 5.2 (c)**, was examined using the TEM analysis. The $MnMoSe_2$/ppy particles are sporadically covered with ppy fibers. The results of FE-SEM study support the idea that this distinct shape increases the surface area, that provides more reactive intermediate active sites for possible interactions. A mixture of distinct spots and ring can be seen in the SAED pattern from a particular location of the material, as shown in **Figure 5.2 (d)**. This pattern highlights the structural complexity of the material by showing that the $MnMoSe_2$/ppy composite has both polycrystalline and amorphous properties. Additionally, from **Figure 5.2 (e)**, HR-TEM image shows distinct lattice fringes that correspond to the (002) plane of the composite material which is already confirmed by the XRD patterns.

5.5.2. Electrochemical characterizations

5.5.2.1. OER study

A range of electrochemical methods, such as LSV, CV, EIS, and Tafel slope analysis, were used to thoroughly assess the efficacy of the produced catalysts for the OER. To guarantee uniform and repeatable electrochemical activity, the electrodes underwent a stabilization step that included 20 cycles of CV before the experimental procedures began. This initial stage is essential because this makes it possible to eliminate any surface contaminants and makes it easier for a stable electroactive layer to develop, which improves the accuracy of the measurements that follow. The LSV plots for the produced catalysts are shown in **Figure 5.5 (a)**, which was conducted at 0.5 mV s^{-1} scan rate. Interestingly, when compared to its constituent parts, the $MnMoSe_2$/ppy composite exhibits the maximum current density and the minimum overpotential **(Figure 5.5 (c))**. The better surface engineering and increased roughness linked to the heterostructure are responsible for this performance improvement, since they effectively increase the number of reactive intermediate active sites that could be availed for the adsorption of OER intermediate species. The FE-SEM image in **Figure 5.2 (b)** provide more evidence for this finding. Both true current density and specific current density (current density per mg of catalyst) were used to evaluate the catalytic activity normalized by electrode roughness factor (R_f) and material loading on the supporting electrode (FTO), respectively. The $MnMoSe_2$/ppy composite's inherent electrochemical activity in supporting the OER could be better understood with this normalizing approach, which guarantees a more accurate comparison of the catalytic performance across various materials [49].

Specific current density (j_{spec}), true current density (j_{true}), along with apparent current density (j_{app}) for the prepared catalysts are shown in **Table 5.2**, together with the associated calculated overpotentials (**Equation 1.19** from **Chapter 1**) at specified current densities. With normalization carried out by the oxide roughness factor or the electrode's geometric surface area, both j_{true} and j_{app} could accurately depict the rate of alkaline water oxidation. According to **Table 5.2**, the overpotentials (η) for the FTO/$MnMoSe_2$/ppy and FTO/$MnMoSe_2$ catalysts were around 205 mV and 303 mV, respectively. Especially when compared to the overpotential of cutting-edge catalysts like RuO_2, which is around 240 mV, these values are competitive. The produced catalysts' potential efficacy in promoting the oxygen evolution process is highlighted by this well alignment, which positions them as viable substitutes for traditional catalysts [50].

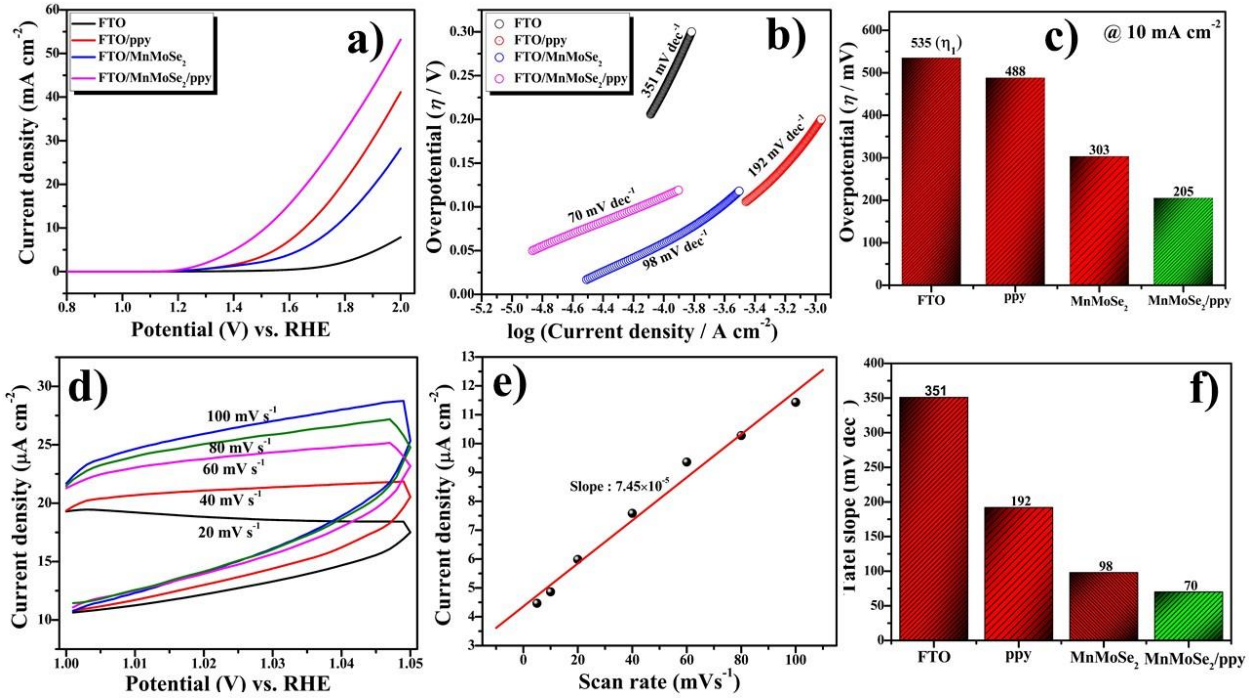

Figure 5.5. a) LSV overlay of prepared electrodes at a scan rate of 0.5 mV s^{-1} in 1 M KOH at room temperature, **b)** Tafel slopes, **c)** Overpotential variation with the prepared catalysts and bare electrode, **d)** CV of FTO/$MnMoSe_2$/ppy electrode in non-faradaic region at varying scan rates, **e)** C_{dl} plot for FTO/$MnMoSe_2$/ppy electrode **f)** Tafel slope variation with the prepared catalysts and bare electrode.

We also determined the catalysts' roughness factor (R_f) and electrochemically active surface area (ECSA) in this investigation. Important knowledge on the distribution and structure of active sites on the electrode facade can be given by the R_f value. A larger surface area that improves adsorption capacity and indicates a more conducive environment for catalytic activity is indicated by a R_f value larger than 1. The catalysts' performance in OER can be greatly enhanced by this increased roughness. To maximize the electrochemical effectiveness of catalysts and optimize their design, it is important to comprehend these factors

[51]. Using the proper calculations, the ECSA was determined (**Equation 1.22** from **Chapter 1**). As seen in **Table 5.2**, the $MnMoSe_2$/ppy composite outperformed the other catalysts with a greater double layer capacitance (C_{dl}) of 41.60 μF cm^{-2} and an ECSA of 0.52 cm^2. This suggests a surface area that is more electrochemically active. The composite material appears to have greater exposure of active sites, that are essential for the electrolysis process, based on the higher ECSA values. The overall catalytic efficacy in the OER is improved by these active sites, which enable effective electron-proton coupled interaction between the electrode and the electrolyte [52]. CV was used to determine the double layer capacitance (C_{dl}) in the non-faradaic area, between 1.00 V to 1.05 V vs. RHE, at varying scan rates between 20 mV s^{-1} to 100 mV s^{-1} **(Figure 5.5 (d))**. A linear graph was obtained by plotting the resultant data as scan rate vs. current density **(Figure 5.5 (e)). Equation 1.23** from **Chapter 1** states that the measurement of C_{dl} is obtained by halving the slope of this straight line. This method makes it possible to accurately evaluate the electrochemical double layer capacitance, which is essential for figuring out the catalysts' electroactive surface area [53].

Table 5.2. Electrode kinetic parameters

Electrode	Overpotential (mV) at 10 mA cm^{-2}	Current density at E = 2 V ($mA\ cm^{-2}$)			C_{dl} ($\mu F\ cm^{-2}$)	R_f	ECSA (cm^2)	Tafel Slope ($mV\ dec^{-1}$)
		j_{app}	j_{true}	$j_{specific}$				
Bare	535 (η_1)	4.87	4.68	14.75	25.02	0.62	0.31	351
FTO/ppy	488	31.31	35.91	94.88	34.88	0.87	0.44	192
FTO/$MnMoSe_2$	303	47.63	76.15	144.33	37.26	0.93	0.46	98
FTO/$MnMoSe_2$/ppy	205	53.06	56.96	160.79	41.60	1.04	0.52	70

The analytical Tafel equation, which is written as $\eta = b \log j$, where η stands for the overpotential, j for the current density, and b for the Tafel slope, was used to calculate the Tafel slope, a crucial measure of catalytic activity. This connection makes it possible to measure the oxygen evolution reaction's kinetics, which sheds light on the catalysts' effectiveness. Tafel slope is a powerful measurement for assessing the effectiveness of the synthesized materials since it often denotes quicker kinetics and improved catalytic activity [54]. With a much lower Tafel slope of 70 mV dec^{-1} **(Figure 5.5 (b))**, the $MnMoSe_2$/ppy composite demonstrated the best catalytic activity when compared to its individual counterparts. The better kinetics of

$MnMoSe_2$/ppy in comparison to the other produced catalysts are highlighted by the measured Tafel slope **(Figure 5.5 (f))**.

The removal of water (H_2O) and the creation of the adsorbed oxygen intermediate (O*), as described in **Equation 4.2** from **Chapter 4** of the OER mechanism, may be the rate-determining step in the OER, given the closeness of the calculated Tafel slope of 70 mV dec^{-1} to the thermodynamic value of 60 mV dec^{-1}. This alignment shows that the $MnMoSe_2$/ppy composite enhances its overall catalytic efficiency by efficiently facilitating this crucial step. The significance of tailoring catalytic materials to target certain reaction pathways in electrochemical processes is shown by the strong agreement between the observed Tafel slope and the predicted value [55]. The Nyquist plots further corroborated the $MnMoSe_2$/ppy composite's improved current density and decreased Tafel slope, confirming that it had the least charge transfer resistance (R_{ct}) among the other variations. This result suggests enhanced electrochemical performance.

We used EIS, which is visually represented in the Nyquist plots **(Figure 5.6 (a))**, to assess the rate of charge transfer between the adsorbed intermediates and the electrode interface. Resistance to charge transfer (R_{ct}) is usually shown by the emergence of a semicircle on the Z_{real} axis, whereas the solution resistance is represented by the curvature coming from the origin. This composite further validates its higher catalytic activity in the oxygen evolution by facilitating quicker charge transfer processes, as seen by the smaller semicircle found for $MnMoSe_2$/ppy [56]. The $MnMoSe_2$/ppy material showed the smallest diameter of a semicircle curvature in the Nyquist plots when compared to $MnMoSe_2$ and ppy. This feature suggests that OER has a lower barrier to charge transfer for composite material. The improved pore design

of the composite, which promotes a larger concentration of charge close to the electrode surface, may be responsible for this increase in charge transfer efficiency. These structural characteristics further assist the enhanced catalytic activity of $MnMoSe_2$/ppy by improving the accessibility of active sites and the electrochemical process's overall kinetics.

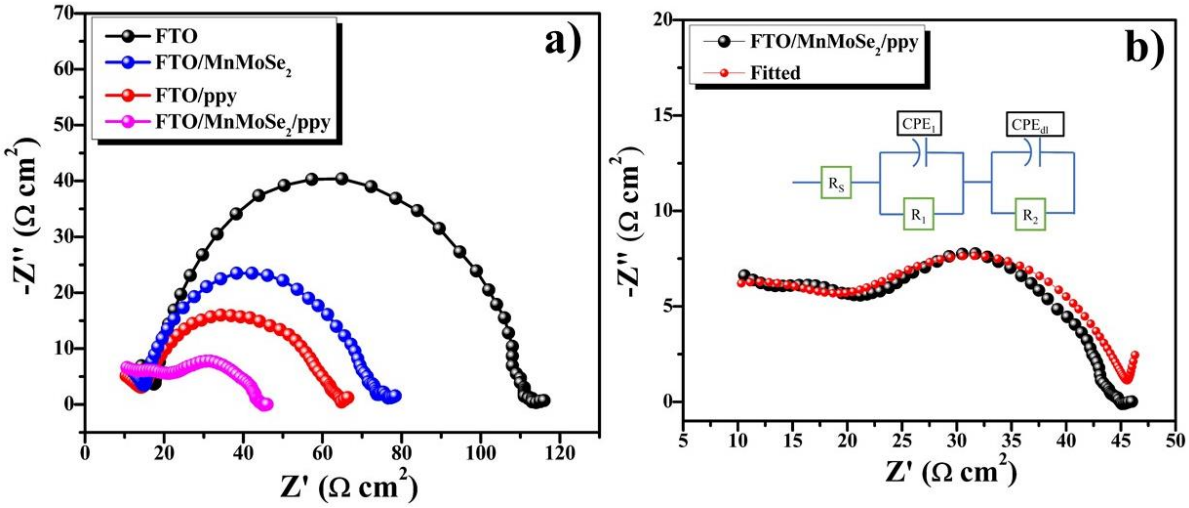

Figure 5.6. a) Nyquist plots at 1.25 V (vs. RHE), **b)** Fitted Nyquist plot of FTO/$MnMoSe_2$/ppy electrode.

The charge transfer resistance (R_{ct}) and the adsorption and desorption processes of reactive intermediate species (H^+/OH^-) are both reflected in the semicircles seen in the Nyquist plots over a range of frequency. These EIS results give a thorough understanding of the materials' catalytic performance and are in excellent alignment with the findings of LSV studies. An analogous circuit model serves as the foundation for the Nyquist plot analysis, as seen in the **Figure 5.6 (b)** inset. The solution resistance is represented by R_s in this model, the charge transfer resistance is indicated by R_{ct}, and the electrode surface resistance from the catalyst to the electrode at the interface is shown by R_1. When combined, these factors provide

a thorough insight of the catalysts' electrochemical behavior. [57]. Generally, a faster electron transfer process is indicated by a smaller R_{ct} value. The $MnMoSe_2$/ppy composite has the lowest R_{ct} value (24.61 Ω), according to the analysis of the fitting data, whereas the R_{ct} values for $MnMoSe_2$ and ppy are 62.68 Ω and 50.70 Ω, respectively. This notable distinction indicates that $MnMoSe_2$/ppy attains maximum catalytic activity and charge transfer efficiency.

By lowering the R_{ct} at the electrolyte-electrode interface, such synergistic actions enhance total charge transport efficiency and minimize interfacial resistance. These results highlight how well the $MnMoSe_2$/ppy combination promotes successful electrochemical reactions. **Table 5.3** contains additional circuit parameters for the comparison.

Table 5.3. Circuit parameters

Electrode	**Solution resistance (R_s) (Ω)**	**Electron transfer resistance (R_1) (Ω)**	**Charge transfer resistance (R_2) (Ω)**
Bare	4.99	13.35	99.14
FTO/ppy	7.81	8.65	50.70
FTO/$MnMoSe_2$	4.94	11.15	62.68
FTO/$MnMoSe_2$/ppy	9.12	13.93	24.61

5.5.2.2. Thermodynamic study

The standard electrochemical activation parameters such as the standard electrochemical energy of activation ($\Delta H_{el}^{0\neq}$), the standard entropy of activation ($\Delta S^{0\neq}$), and the standard enthalpy of activation ($\Delta H^{0\neq}$) were determined by examining electrodes fabricated of FTO/$MnMoSe_2$/ppy, FTO/$MnMoSe_2$, FTO/ppy, and bare FTO. A 1 M KOH electrolyte was used to record anodic polarization curves between 25 to 55 ^oC. To provide stable reference conditions, the reference electrode was maintained at a steady 25 °C during the whole experiment **(Figure 5.7 (a))**. Following the construction of corresponding Arrhenius plots **(Figure 5.7 (b))**, **Table 5.4** summarized the comparison findings for $MnMoSe_2$ and ppy. Among the materials examined, the FTO/$MnMoSe_2$/ppy electrode showed the lowest electrochemical activation energy, as expected. This result suggests that, in comparison to the others, the composite requires less energy to promote the reaction. The average transfer coefficient α for $MnMoSe_2$/ppy almost reached unity, indicating efficient electron transport, using the formula $\alpha = 2.303RT/bF$, where b is the tafel slope, T is the absolute temperature, F is the Faraday constant, and R is the gas constant.

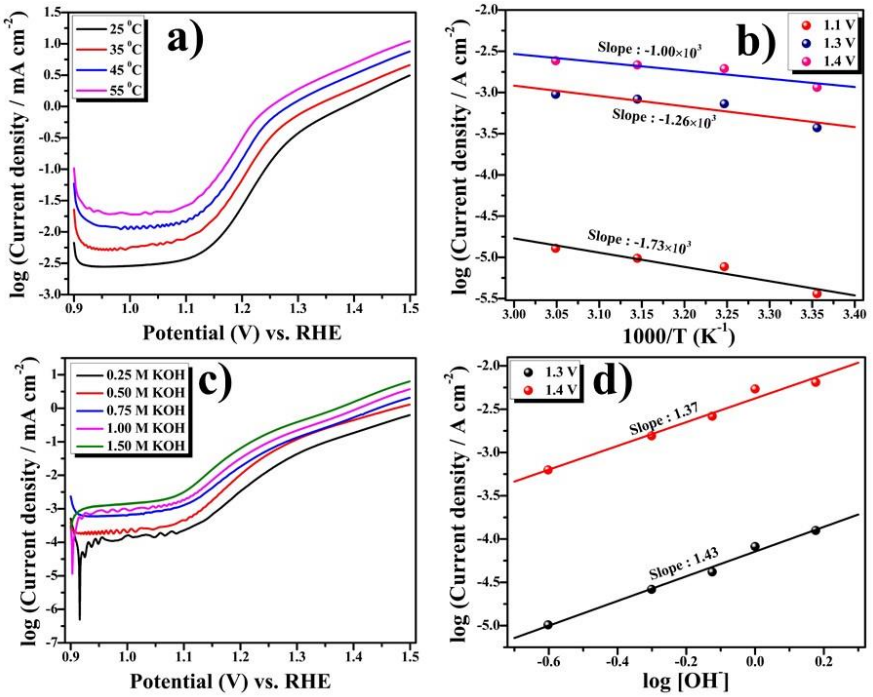

Figure 5.7. a) Tafel polarization plots of FTO/$MnMoSe_2$/ppy electrode at varying temperatures, **b)** Arrhenius plot, **c)** Tafel polarization plots of FTO/$MnMoSe_2$/ppy electrode at varying concentrations of KOH **d)** reaction order.

Table 5.4 provides the average values of thermodynamic parameters that are computed using established equations **(Equations 1.27 and 1.29** from **Chapter 1)**. According to the polarization curves acquired at various temperatures, the Tafel slope (b), given in mV dec^{-1}, was calculated. In addition, the frequency term was modified to include the Boltzmann constant (k_B), and the Planck's constant (h). In terms of electrochemical oxygen production, the findings show that the FTO/$MnMoSe_2$/ppy electrode has the highest rate of adsorption, suggesting that there are more active sites available for reactive species adsorption. This is suggested from increased catalytic activity and is consistent with the highest negative value of $\Delta S^{0\neq}$. **Table 5.4** lists complete thermodynamic parameters that were determined using the

approach presented [58]. All the plots made for $MnMoSe_2$ catalyst are given below in **Figure 5.8.**

Table 5.4. Thermodynamic parameters

Electrode	Standard electrochemical energy of activation ($\Delta H_{el}^{0\neq}$) (kJ mol^{-1})	Standard electrochemical entropy of activation ($-\Delta S_{el}^{0\neq}$) (J K^{-1}mol^{-1})	Transfer coefficient (α)	Standard enthalpy of activation ($\Delta H^{0\neq}$) (kJ mol^{-1})
Bare	50.28	42.31	0.17	181.31
FTO/ppy	47.90	67.97	0.31	153.32
FTO/$MnMoSe_2$	37.52	88.65	0.60	110.11
FTO/$MnMoSe_2$/ppy	19.19	159.69	0.84	80.71

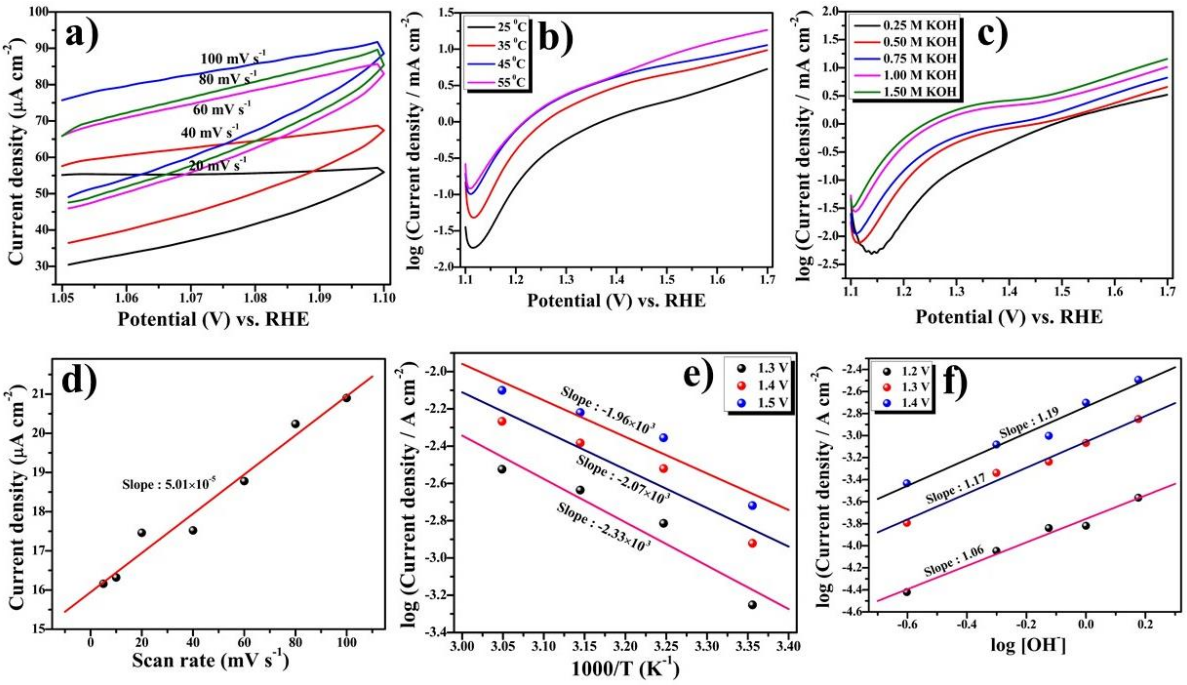

Figure 5.8. a) CV of FTO/$MnMoSe_2$ electrode in non-faradaic region at different scan rates, **b)** Tafel polarization curves of FTO/$MnMoSe_2$ electrode at different temperatures, **c)** Tafel polarization curves of FTO/$MnMoSe_2$ electrode at different concentrations of KOH, **d)** Corresponding C_{dl} plot for FTO/$MnMoSe_2$ electrode, **e)** Corresponding Arrhenius plot for FTO/$MnMoSe_2$ electrode, **f)** order of reaction for FTO/$MnMoSe_2$ electrode.

5.5.2.3. OER mechanism

From the previously reported methods [59], by altering the concentration of OH^- ions, the order of reaction was examined. Non-integer values were detected for each catalyst, which is not unusual and has been documented in a number of investigations in the literature [60,61]. Complex kinetics and the presence of several stages or intermediates in the electrochemical process might result in such non-integer reaction orders. These results demonstrate the

complexity of the OER process and the need for more research to completely comprehend the catalytic dynamics at work. By taking into account the adsorption and ionization of OH^- ions on surface hydroxyl groups, this behavior may be explained. The observed non-integer reaction ordering could be responsible to the interaction between the hydroxide ions and the surface species, which can also affect the reaction kinetics. specifically, the stability of intermediates in the OER as well as the adsorption energies can be significantly impacted by the production and reactivity of surface hydroxyl groups during the electrocatalytic process. The intricacy of the electrochemical environment and the significance of comprehending how surface chemistry affects catalytic performance are highlighted by such interactions [62]. Furthermore, the reaction kinetics can be strongly impacted by the overall facade covering of adsorbed intermediates, particularly oxygen-containing species produced in the electrochemical production of molecular oxygen. A linear connection between the adsorption energy and the degree of coverage characterizes the interaction of these species with the catalyst surface under Temkin adsorption conditions. This implies that the energy involved in further adsorption varies with the number of intermediates adsorbed, affecting the OER overall kinetics. When assessing the performance of electrocatalysts, it is important to take into account the complex interactions between surface species and reaction conditions, since these surface coverage effects might result in differences in catalytic activity and efficiency [63,64]. To ascertain the reaction sequence in the OER, Tafel polarization curves were acquired for every electrode that was constructed. This work used a neutral electrolyte, KNO_3, to maintain a consistent ionic strength. Polarization plots obtained at different KOH concentrations at various potentials were

examined in order to create linear log (current density) vs. log [OH^-] plots and from these curves the sequence of responses was then ascertained by calculating these straight lines' slope.

One proton transfer in basic solution is one of the four electrochemical stages that normally make up the OER process (Adsorbate Evolution Mechanism (AEM)). The electro-sorption of OH^- ions **(Equation (4.1)** from **Chapter 4)** follows the adsorption and desorption of OH^- ions at the metal's (M) active sites, where the process starts. Then, as indicated by M-O bonding, an O-O bond is made via a sequence of intermediate species, such as OH*, O*, OOH*, and OO*, which are adsorbed onto the metal's active sites (as illustrated in **Equations 4.2, 4.3,** and **4.4** from **Chapter 4)**. From previous studies, these chemical processes are essential to the OER mechanism, emphasizing the intricate interactions that take place between the many intermediates and the catalyst surface throughout the reaction [54,65] (Detailed discussion in **Chapter 1**).

$$OH^- + M \rightarrow M + OH^* + e^- \quad \textbf{(4.1)}$$

$$OH^* + OH^- \rightarrow O^* + H_2O + e^- \quad \textbf{(4.2)}$$

$$OH^- + O^* \rightarrow OOH^* + e^- \quad \textbf{(4.3)}$$

$$OH^- + OOH^* \rightarrow O_2 + H_2O + e^- \quad \textbf{(4.4)}$$

This process is as same as the Bockris' electrochemical pathway [63]. However, it's critical to acknowledge the likely existence of other paths, such Krasil'shchikov's pathway and Bockris-Otagawa's peroxide route [63]. In the suggested mechanism, 'M' (Mn, Mo) functions as the active site on the electrode surface, while OH* and O* operate as surface-adsorbed intermediate species.

Notably, at high pH conditions, the selenide component acts as a "pre-catalyst" for the OER. According to research, some of the manganese and Mo from $MnMoSe_2$ is converted to MnOOH and MoOOH at the catalyst surface, where it functions as the active catalyst during the OER. This change demonstrates the materials' dual function, since the first pre-catalytic phase results in the creation of an active species that improves catalytic activity in alkaline environments. This kind of activity emphasizes how important the chemical and structural characteristics of selenide are for promoting effective electrochemical reactions [66].

5.5.2.4. Stability and durability

A catalyst must have both exceptional catalytic activity and long-term stability during extended usage in order to be deemed practically appropriate and economically successful. Thus, it is crucial to assess an electrocatalyst's stability and longevity. In this investigation, chronopotentiometry measurements in a 1 M KOH electrolyte were used to evaluate the stability of the FTO/$MnMoSe_2$/ppy electrode. The FTO/$MnMoSe_2$/ppy electrode demonstrated exceptional stability over a 12-hour period, as shown in **Figure 5.9**, with no discernible change in potential. This steady performance shows that even when gas bubbles evolve during the OER, the electrode successfully maintains its catalytic activity. Any electrocatalyst must have this stability, which emphasizes the FTO/$MnMoSe_2$/ppy composite's applicability for real-world uses.

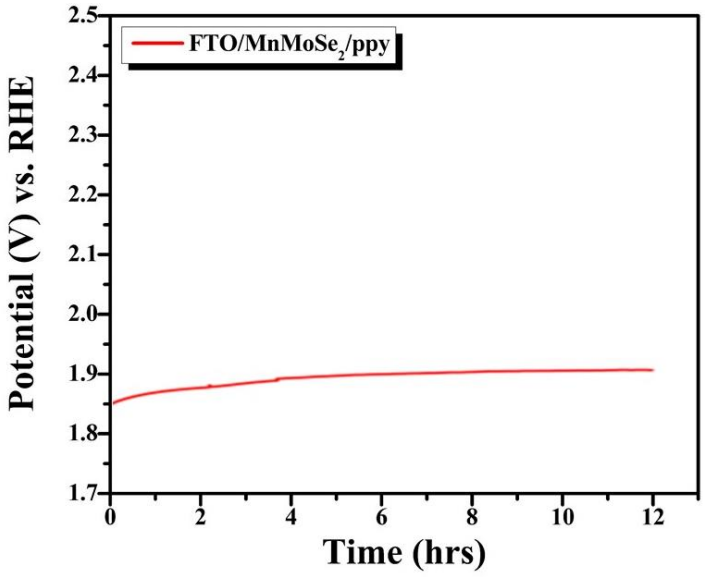

Figure 5.9. Chronopotentiometry test at 10 mA cm^{-2}.

5.5.3. *Operando* Spectro-electrochemical study

In UV-Vis spectro-electrochemistry (SEC), absorbance is measured as well as the circuit's current is simultaneously tracked. This method makes it possible to correlate changes in electrolyte surroundings and reaction conditions with optical and current responses in proportion to the applied potential. UV-Vis SEC may be used to electrode materials, although its main application has been in the investigation of molecular systems. This method is usually used in a three-electrode cell setup to study certain redox processes. This configuration offers insights into the variations in absorbance linked to the electrochemical processes occurring at the electrode surface and permits exact control over the voltage applied to the working electrode [67].

Figure 5.10 shows the *operando* UV-Vis spectroscopy performed at 5 mV s^{-1} scan rate before and during LSV for the FTO/$MnMoSe_2$/ppy electrode at room temperature in a 1 M

KOH electrolyte. Different absorption peaks appeared in the 300–440 nm region and a smaller peak was seen between 850 and 900 nm as the electrode potential was stepped from 1.2 V to 2.2 V vs. RHE in increments of 0.1 V. Interestingly, when the applied voltage increased, these absorbance peaks not only widened but also became more intense. These spectrum characteristics are probably linked to the development of MnOOH species, indicating that these intermediates are produced as a result of the electrode surface's electrochemical activation during OER [68].

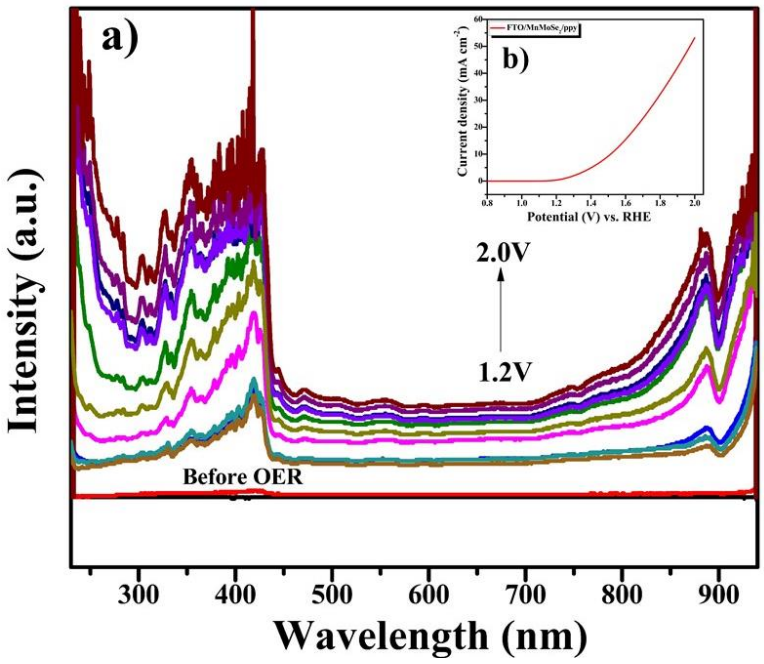

Figure 5.10. *Operando* UV-vis spectra of FTO/$MnMoSe_2$/ppy operating at 5 mV s^{-1} scan rate during LSV.

5.6. Conclusion

The efficiency of the catalysts for alkaline water oxidation was assessed. According to the experimental results, $MnMoSe_2$/ppy may be easily and affordably manufactured by a hydrothermal approach accompanied by solid-state grinding. The FTO/$MnMoSe_2$/ppy electrode showed the least Tafel slope among other catalysts evaluated, showing its higher electrocatalytic performance for alkaline water oxidation. For the OER process, this catalyst showed kinetics that were almost first-order. Its effectiveness was further supported by the fact that $MnMoSe_2$/ppy possess the least standard electrochemical energy of activation among the catalysts evaluated. The production of absorption peaks in the 300–440 nm region, which were ascribed to the MnOOH intermediate, demonstrated the active sites for OER by means of *operando* spectro-electrochemical analysis. More research in the near-infrared (NIR) spectrum is necessary to completely clarify the function of these redox-active sites. Additionally, it has been found that many redox species are produced during the OER, with the huge enhancement of the electrocatalytic activity of $MnMoSe_2$/ppy, the material with the maximum absorbance intensity. Furthermore, $MnMoSe_2$/ppy show a lot of potential as electrode materials for energy storage devices and other uses. Industrial-scale feasible water splitting might be accomplished by using effective OER catalysts, supplying the pure and effective fuel required to satisfy current needs.

5.7. Reference

[1] M. Child, C. Breyer, Transition and transformation: A review of the concept of change in the progress towards future sustainable energy systems, Energy Policy 107 (2017) 11–26. https://doi.org/10.1016/j.enpol.2017.04.022.

[2] M. Wiechen, M.M. Najafpour, S.I. Allakhverdiev, L. Spiccia, Water oxidation catalysis by manganese oxides: Learning from evolution, Energy Environ. Sci. 7 (2014) 2203–2212. https://doi.org/10.1039/c4ee00681j.

[3] A. Kalair, N. Abas, M.S. Saleem, A.R. Kalair, N. Khan, Role of energy storage systems in energy transition from fossil fuels to renewables, Energy Storage 3 (2021). https://doi.org/10.1002/est2.135.

[4] T. Guo, L. Li, Z. Wang, Recent Development and Future Perspectives of Amorphous Transition Metal-Based Electrocatalysts for Oxygen Evolution Reaction, Adv. Energy Mater. 12 (2022). https://doi.org/10.1002/aenm.202200827.

[5] V.J. Babu, M.K. Kumar, A.S. Nair, T.L. Kheng, S.I. Allakhverdiev, S. Ramakrishna, Visible light photocatalytic water splitting for hydrogen production from N-TiO 2 rice grain shaped electrospun nanostructures, Int. J. Hydrogen Energy 37 (2012) 8897–8904. https://doi.org/10.1016/j.ijhydene.2011.12.015.

[6] G.B. Darband, M. Aliofkhazraei, S. Shanmugam, Recent advances in methods and technologies for enhancing bubble detachment during electrochemical water splitting, Renew. Sustain. Energy Rev. 114 (2019). https://doi.org/10.1016/j.rser.2019.109300.

[7] M. Otto, K.L. Chagoya, R.G. Blair, S.M. Hick, J.S. Kapat, Optimal hydrogen carrier: Holistic evaluation of hydrogen storage and transportation concepts for power generation, aviation, and transportation, J. Energy Storage 55 (2022). https://doi.org/10.1016/j.est.2022.105714.

[8] M.M. Najafpour, S.I. Allakhverdiev, Manganese compounds as water oxidizing catalysts for hydrogen production via water splitting: From manganese complexes to nano-sized manganese oxides, Int. J. Hydrogen Energy 37 (2012) 8753–8764. https://doi.org/10.1016/j.ijhydene.2012.02.075.

[9] B. Xiong, L. Chen, J. Shi, Anion-Containing Noble-Metal-Free Bifunctional Electrocatalysts for Overall Water Splitting, ACS Catal. 8 (2018) 3688–3707. https://doi.org/10.1021/acscatal.7b04286.

[10] Y. Shi, B. Zhang, Recent advances in transition metal phosphide nanomaterials: Synthesis and applications in hydrogen evolution reaction, Chem. Soc. Rev. 45 (2016)

1529–1541. https://doi.org/10.1039/c5cs00434a.

[11] S. Kalantarifard, S.I. Allakhverdiev, M.M. Najafpour, Water oxidation by a nickel complex: New challenges and an alternative mechanism, Int. J. Hydrogen Energy 45 (2020) 33563–33573. https://doi.org/10.1016/j.ijhydene.2020.09.111.

[12] H. Feizi, R. Bagheri, Z. Song, J.R. Shen, S.I. Allakhverdiev, M.M. Najafpour, Cobalt/Cobalt Oxide Surface for Water Oxidation, ACS Sustain. Chem. Eng. 7 (2019) 6093–6105. https://doi.org/10.1021/acssuschemeng.8b06269.

[13] M. Khosravi, H. Feizi, B. Haghighi, S.I. Allakhverdiev, M.M. Najafpour, Investigation of photo-electrochemical response of iron oxide/mixed-phase titanium oxide heterojunction toward possible solar energy conversion, Int. J. Hydrogen Energy 46 (2021) 7241–7253. https://doi.org/10.1016/j.ijhydene.2020.11.247.

[14] Q. Lu, Y. Yu, Q. Ma, B. Chen, H. Zhang, 2D Transition-Metal-Dichalcogenide-Nanosheet-Based Composites for Photocatalytic and Electrocatalytic Hydrogen Evolution Reactions, Adv. Mater. 28 (2016) 1917–1933. https://doi.org/10.1002/adma.201503270.

[15] H. Shu, D. Zhou, F. Li, D. Cao, X. Chen, Defect Engineering in MoSe2 for the Hydrogen Evolution Reaction: From Point Defects to Edges, ACS Appl. Mater. Interfaces 9 (2017) 42688–42698. https://doi.org/10.1021/acsami.7b12478.

[16] H.P. Komsa, A. V. Krasheninnikov, Native defects in bulk and monolayer MoS2 from first principles, Phys. Rev. B - Condens. Matter Mater. Phys. 91 (2015) 125304. https://doi.org/10.1103/PhysRevB.91.125304.

[17] A. Shafqat, T. Iqbal, A. Majid, A DFT study of intrinsic point defects in monolayer MoSe2, AIP Adv. 7 (2017). https://doi.org/10.1063/1.4999524.

[18] A.A. Tedstone, D.J. Lewis, P. O'Brien, Synthesis, Properties, and Applications of Transition Metal-Doped Layered Transition Metal Dichalcogenides, Chem. Mater. 28 (2016) 1965–1974. https://doi.org/10.1021/acs.chemmater.6b00430.

[19] X. Chen, Y. Qiu, G. Liu, W. Zheng, W. Feng, F. Gao, W. Cao, Y. Fu, W. Hu, P. Hu, Tuning electrochemical catalytic activity of defective 2D terrace MoSe2 heterogeneous catalyst: Via cobalt doping, J. Mater. Chem. A 5 (2017) 11357–11363. https://doi.org/10.1039/c7ta02327h.

[20] T. Tian, H. Gao, X. Zhou, L. Zheng, J. Wu, K. Li, Y. Ding, Study of the Active Sites in Porous Nickel Oxide Nanosheets by Manganese Modulation for Enhanced Oxygen Evolution Catalysis, ACS Energy Lett. 3 (2018) 2150–2158. https://doi.org/10.1021/acsenergylett.8b01206.

[21] Y. Liu, X. Hua, C. Xiao, T. Zhou, P. Huang, Z. Guo, B. Pan, Y. Xie, Heterogeneous Spin States in Ultrathin Nanosheets Induce Subtle Lattice Distortion to Trigger Efficient Hydrogen Evolution, J. Am. Chem. Soc. 138 (2016) 5087–5092. https://doi.org/10.1021/jacs.6b00858.

[22] L. Lin, N. Miao, Y. Wen, S. Zhang, P. Ghosez, Z. Sun, D.A. Allwood, Sulfur-Depleted Monolayered Molybdenum Disulfide Nanocrystals for Superelectrochemical Hydrogen Evolution Reaction, ACS Nano 10 (2016) 8929–8937. https://doi.org/10.1021/acsnano.6b04904.

[23] C. Xu, S. Peng, C. Tan, H. Ang, H. Tan, H. Zhang, Q. Yan, Ultrathin S-doped MoSe2 nanosheets for efficient hydrogen evolution, J. Mater. Chem. A 2 (2014) 5597–5601. https://doi.org/10.1039/c4ta00458b.

[24] M. Kan, S. Adhikari, Q. Sun, Ferromagnetism in MnX2 (X = S, Se) monolayers, Phys. Chem. Chem. Phys. 16 (2014) 4990–4994. https://doi.org/10.1039/c3cp55146f.

[25] N. Elliott, The Crystal Structure of Manganese Diselenide and Manganese Ditelluride, J. Am. Chem. Soc. 59 (1937) 1958–1962. https://doi.org/10.1021/ja01289a049.

[26] O. Goede, W. Heimbrodt, Optical Properties of (Zn, Mn) and (Cd, Mn) Chalcogenide Mixed Crystals and Superlattices, Phys. Status Solidi 146 (1988) 11–62. https://doi.org/10.1002/pssb.2221460102.

[27] A. Sobhani, M. Salavati-Niasari, Hydrothermal synthesis, characterization, and magnetic properties of cubic MnSe2/Se nanocomposites material, J. Alloys Compd. 617 (2014) 93–101. https://doi.org/10.1016/j.jallcom.2014.08.013.

[28] J. Zhang, J. Liu, C. Liang, F. Zhang, R. Che, Highly crystalline manganese selenide nanorods: Synthesis, characterization, and microwave absorption properties, J. Alloys Compd. 548 (2013) 13–17. https://doi.org/10.1016/j.jallcom.2012.09.025.

[29] G.A. Tigwere, M.D. Khan, L.D. Nyamen, F.M. de Souza, W. Lin, R.K. Gupta, N. Revaprasadu, P.T. Ndifon, Transition metal (Ni, Cu and Fe) doped MnS nanostructures: Effect of doping on supercapacitance and water splitting, Mater. Sci. Semicond. Process. 158 (2023). https://doi.org/10.1016/j.mssp.2023.107365.

[30] J. Kundu, S. Khilari, K. Bhunia, D. Pradhan, Ni-Doped CuS as an efficient electrocatalyst for the oxygen evolution reaction, Catal. Sci. Technol. 9 (2019) 406–417. https://doi.org/10.1039/c8cy02181c.

[31] R. Kumar, A. Sudhaik, Sonu, P. Raizada, V.H. Nguyen, Q. Van Le, T. Ahamad, S. Thakur, C.M. Hussain, P. Singh, Integrating K and P co-doped g-C3N4 with ZnFe2O4 and graphene oxide for S-scheme-based enhanced adsorption coupled photocatalytic

real wastewater treatment, Chemosphere 337 (2023). https://doi.org/10.1016/j.chemosphere.2023.139267.

[32] D. Liu, P. Zhou, H. Bai, H. Ai, X. Du, M. Chen, D. Liu, W.F. Ip, K.H. Lo, C.T. Kwok, S. Chen, S. Wang, G. Xing, X. Wang, H. Pan, Development of Perovskite Oxide-Based Electrocatalysts for Oxygen Evolution Reaction, Small 17 (2021). https://doi.org/10.1002/smll.202101605.

[33] H. Wu, W. Xiao, C. Guan, X. Liu, W. Zang, H. Zhang, J. Ding, Y.P. Feng, S.J. Pennycook, J. Wang, Hollow Mo-doped CoP nanoarrays for efficient overall water splitting, Nano Energy 48 (2018) 73–80. https://doi.org/10.1016/j.nanoen.2018.03.034.

[34] H. Tsai, R. Asadpour, J.C. Blancon, C.C. Stoumpos, O. Durand, J.W. Strzalka, B. Chen, R. Verduzco, P.M. Ajayan, S. Tretiak, J. Even, M.A. Alam, M.G. Kanatzidis, W. Nie, A.D. Mohite, Light-induced lattice expansion leads to high-efficiency perovskite solar cells, Science (80-.). 360 (2018) 67–70. https://doi.org/10.1126/science.aap8671.

[35] M. Sadaqat, S. Manzoor, L. Nisar, A. Hassan, D. Tyagi, J.H. Shah, M.N. Ashiq, K.S. Joya, T. Alshahrani, M. Najam-ul-Haq, Iron doped nickel ditelluride hierarchical nanoflakes arrays directly grown on nickel foam as robust electrodes for oxygen evolution reaction, Electrochim. Acta 371 (2021). https://doi.org/10.1016/j.electacta.2021.137830.

[36] W. Wang, F. Xiong, S. Zhu, J. Chen, J. Xie, Q. An, Defect engineering in molybdenum-based electrode materials for energy storage, EScience 2 (2022) 278–294. https://doi.org/10.1016/j.esci.2022.04.005.

[37] A. Bahloul, B. Nessark, E. Briot, H. Groult, A. Mauger, K. Zaghib, C.M. Julien, Polypyrrole-covered MnO2 as electrode material for supercapacitor, J. Power Sources 240 (2013) 267–272. https://doi.org/10.1016/j.jpowsour.2013.04.013.

[38] L. Liu, Y. Hou, J. Wang, J. Chen, H.K. Liu, Y. Wu, J. Wang, Nanofibrous Co3O4/PPy Hybrid with Synergistic Effect as Bifunctional Catalyst for Lithium-Oxygen Batteries, Adv. Mater. Interfaces 3 (2016) 1600030. https://doi.org/10.1002/admi.201600030.

[39] J. Jiang, W. Shi, S. Song, Q. Hao, W. Fan, X. Xia, X. Zhang, Q. Wang, C. Liu, D. Yan, Solvothermal synthesis and electrochemical performance in super-capacitors of Co3O4/C flower-like nanostructures, J. Power Sources 248 (2014) 1281–1289. https://doi.org/10.1016/j.jpowsour.2013.10.046.

[40] H. Mao, X. Guo, Y. Fu, Z. Cao, D. Sun, B. Wang, Y. Zhang, Q. Fan, X.M. Song, Efficiently improving oxygen evolution activity using hierarchical α-Co(OH)2/polypyrrole/graphene oxide nanosheets, Appl. Surf. Sci. 485 (2019) 554–

563. https://doi.org/10.1016/j.apsusc.2019.04.195.

[41] K. Kawashima, R.A. Márquez, Y.J. Son, C. Guo, R.R. Vaidyula, L.A. Smith, C.E. Chukwuneke, C.B. Mullins, Accurate Potentials of Hg/HgO Electrodes: Practical Parameters for Reporting Alkaline Water Electrolysis Overpotentials, ACS Catal. 13 (2023) 1893–1898. https://doi.org/10.1021/acscatal.2c05655.

[42] J.L.H. Chau, M.K. Hsu, C.C. Kao, Microwave plasma synthesis of Co and SiC-coated Co nanopowders, Mater. Lett. 60 (2006) 947–951. https://doi.org/10.1016/j.matlet.2005.10.054.

[43] R.N. Singh, J.P. Pandey, N.K. Singh, B. Lal, P. Chartier, J.F. Koenig, Sol-gel derived spinel MxCo3-xO4 (M = Ni, Cu; 0≤x≤1) films and oxygen evolution, Electrochim. Acta 45 (2000) 1911–1919. https://doi.org/10.1016/S0013-4686(99)00413-2.

[44] R.N. Singh, J.P. Singh, B. Lal, M.J.K. Thomas, S. Bera, New NiFe2-xCrxO4 spinel films for O2 evolution in alkaline solutions, Electrochim. Acta 51 (2006) 5515–5523. https://doi.org/10.1016/j.electacta.2006.02.028.

[45] H. Ai, L. Fan, Y. Wang, Z. Wang, H. Zhang, J. Zhao, M. Jiao, B. Lv, X. Han, OER catalytic performance of a composite catalyst comprising multi-layer thin flake Co3O4 and PPy nanofibers, RSC Adv. 13 (2023) 32045–32053. https://doi.org/10.1039/d3ra05936g.

[46] S. Ramaraj, M. Sakthivel, S.M. Chen, B.S. Lou, K.C. Ho, Defect and Additional Active Sites on the Basal Plane of Manganese-Doped Molybdenum Diselenide for Effective Enzyme Immobilization: In Vitro and in Vivo Real-Time Analyses of Hydrogen Peroxide Sensing, ACS Appl. Mater. Interfaces 11 (2019) 7862–7871. https://doi.org/10.1021/acsami.8b22389.

[47] M.S. Vidhya, R. Yuvakkumar, P.S. Kumar, G. Ravi, D. Velauthapillai, Hydrothermal Synthesis of Flower Like MnSe2@MoSe2 Electrode for Supercapacitor Applications, Top. Catal. 65 (2022) 615–622. https://doi.org/10.1007/s11244-021-01472-7.

[48] J. Yang, C. Wang, H. Ju, Y. Sun, S. Xing, J. Zhu, Q. Yang, Integrated Quasiplane Heteronanostructures of MoSe2/Bi2Se3 Hexagonal Nanosheets: Synergetic Electrocatalytic Water Splitting and Enhanced Supercapacitor Performance, Adv. Funct. Mater. 27 (2017). https://doi.org/10.1002/adfm.201703864.

[49] A.S. Chaddha, N.K. Singh, M. Malviya, A. Sharma, Birnessite-clay mineral couple in the rock varnish: a nature's electrocatalyst, Sustain. Energy Fuels 6 (2022) 2553–2569. https://doi.org/10.1039/d2se00185c.

[50] S. Pal, U.P. Azad, A.K. Singh, D. Kumar, R. Prakash, Studies on some spinel oxides

based electrocatalysts for oxygen evolution and capacitive applications, Electrochim. Acta 320 (2019) 134584. https://doi.org/10.1016/j.electacta.2019.134584.

[51] A. Hojatshamami, Ni-Co and Ni-Fe Catalysts for The Oxygen Evolution Reaction in Alkaline Water Electrolysis, (2022). https://hdl.handle.net/11250/3042808 (accessed June 23, 2024).

[52] H. Zeng, Y. Zeng, J. Qi, L. Gu, E. Hong, R. Si, C. Yang, The role of proton dynamics on the catalyst-electrolyte interface in the oxygen evolution reaction, Chinese J. Catal. 43 (2022) 139–147. https://doi.org/10.1016/S1872-2067(21)63909-8.

[53] U.J. Awan, M.A. Basit, S.I.A. Shah, J. Yong-Xin, H. Zhifu, Minimized OER overpotential via SILAR-based development of g-C3N4/CdS nanocomposite, Appl. Phys. A Mater. Sci. Process. 129 (2023) 1–15. https://doi.org/10.1007/s00339-023-07105-y.

[54] Z. Hu, L. Hao, F. Quan, R. Guo, Recent developments of Co3O4-based materials as catalysts for the oxygen evolution reaction, Catal. Sci. Technol. 12 (2022) 436–461. https://doi.org/10.1039/d1cy01688a.

[55] R.L. Doyle, M.E.G. Lyons, An electrochemical impedance study of the oxygen evolution reaction at hydrous iron oxide in base, Phys. Chem. Chem. Phys. 15 (2013) 5224–5237. https://doi.org/10.1039/c3cp43464h.

[56] A. Bard, L. Faulkner, H. White, Electrochemical methods: fundamentals and applications, 2022. https://books.google.com/books?hl=en&lr=&id=Sct6EAAAQBAJ&oi=fnd&pg=PR21&ots=QV3mtaJ0NX&sig=DLfrR_jFcE_cWnGqn5_EbKOHFu0 (accessed May 6, 2024).

[57] W. Choi, H.C. Shin, J.M. Kim, J.Y. Choi, W.S. Yoon, Modeling and applications of electrochemical impedance spectroscopy (Eis) for lithium-ion batteries, J. Electrochem. Sci. Technol. 11 (2020) 1–13. https://doi.org/10.33961/jecst.2019.00528.

[58] A.S. Chaddha, N.K. Singh, M. Malviya, A. Sharma, Birnessite-clay mineral couple in the rock varnish: a nature's electrocatalyst, Sustain. Energy Fuels 6 (2022) 2553–2569. https://doi.org/10.1039/D2SE00185C.

[59] R.N. Singh, N.K. Singh, J.P. Singh, Electrocatalytic properties of new active ternary ferrite film anodes for O2 evolution in alkaline medium, Electrochim. Acta 47 (2002) 3873–3879. https://doi.org/10.1016/S0013-4686(02)00354-7.

[60] F. Švegl, B. Orel, I. Grabec-Švegl, V. Kaučič, Characterization of spinel Co3O4 and Li-doped Co3O4 thin film electrocatalysts prepared by the sol-gel route, Electrochim.

Acta 45 (2000) 4359–4371. https://doi.org/10.1016/S0013-4686(00)00543-0.

[61] R.N. Singh, J.F. Koenig, G. Poillerat, P. Chartier, Thin films of CO3O4 and NiCo2O4 prepared by the method of chemical spray pyrolysis for electrocatalysis. Part IV. The electrocatalysis of oxygen reduction, J. Electroanal. Chem. 314 (1991) 241–257. https://doi.org/10.1016/0022-0728(91)85440-Z.

[62] L.I. Krishtalik, Kinetics and mechanism of anodic chlorine and oxygen evolution reactions on transition metal oxide electrodes, Electrochim. Acta 26 (1981) 329–337. https://doi.org/10.1016/0013-4686(81)85019-0.

[63] J.O.M. Bockris, T. Otagawa, Mechanism of oxygen evolution on perovskites, J. Phys. Chem. 87 (1983) 2960–2971. https://doi.org/10.1021/j100238a048.

[64] R.N. Singh, J.F. Koenig, G. Poillerat, P. Chartier, Thin films of CO3O4 and NiCo2O4 prepared by the method of chemical spray pyrolysis for electrocatalysis. Part IV. The electrocatalysis of oxygen reduction, J. Electroanal. Chem. 314 (1991) 241–257. https://doi.org/10.1016/0022-0728(91)85440-Z.

[65] S. Pal, U.P. Azad, A.K. Singh, D. Kumar, R. Prakash, Studies on some spinel oxides based electrocatalysts for oxygen evolution and capacitive applications, Electrochim. Acta 320 (2019). https://doi.org/10.1016/j.electacta.2019.134584.

[66] I.H. Kwak, H.S. Im, D.M. Jang, Y.W. Kim, K. Park, Y.R. Lim, E.H. Cha, J. Park, CoSe2 and NiSe2 Nanocrystals as Superior Bifunctional Catalysts for Electrochemical and Photoelectrochemical Water Splitting, ACS Appl. Mater. Interfaces 8 (2016) 5327–5334. https://doi.org/10.1021/acsami.5b12093.

[67] K.J. Lee, N. Elgrishi, B. Kandemir, J.L. Dempsey, Electrochemical and spectroscopic methods for evaluating molecular electrocatalysts, Nat. Rev. Chem. 1 (2017). https://doi.org/10.1038/s41570-017-0039.

[68] H. Mashiko, K. Yoshimatsu, T. Oshima, A. Ohtomo, Fabrication and Characterization of Semiconductor Photoelectrodes with Orientation-Controlled α-Fe2O3 Thin Films, J. Phys. Chem. C 120 (2016) 2747–2752. https://doi.org/10.1021/ACS.JPCC.5B10838.